Numerical simulation of proppant transport in a planar fracture. A study of perforation placement and injection strategy

Mauro Baldini [a,b,*], C. Manuel Carlevaro [c], Luis A. Pugnaloni [a,*], Martín Sánchez [b]

[a] *Dpto. Ing. Mecánica, Universidad Tecnológica Nacional, Facultad Regional de La Plata, CONICET, Av. 60 Esq. 124, La Plata, 1900, Argentina*
[b] *YPF Tecnología S.A. (Y-TEC), Av. del Petroleo Argentino s/n, Berisso, 1923, Argentina*
[c] *Instituto de Física de Líquidos y Sistemas Biológicos (UNLP, CONICET La Plata), Calle 59 N 789, La Plata, 1900, Argentina*

A B S T R A C T

We present numerical simulations, based on a CFD–DEM approach, of the transport and settlement of proppant in a planar vertical cell that mimics a hydraulic fracture. These simulations, with resolution at the particle level, allow for a clean measurement of the dune placement and proppant degree of mixing. The effect of the position of the injection points is considered by three different injection heights in the vertical cell. Different proppant injection strategies were also considered by using two different proppant types that can be injected in different orders or simultaneously as a mixture. We evaluate the position and shape of the settled dune. We measure the degree of mixing of the two proppant types by using the concept of mixing entropy. We have found that an injection point placed close to the bottom of the cell leads to a dune close to the injection points, and that an injection point at the middle or at the top of the cell leads to a rather flat dune. Injecting different proppant types in different orders yields distinctive proppant distributions. This helps in evaluating the benefits of positioning perforation clusters close to geological boundaries that favor fracture growth in the upward or downward direction as well as selecting the order of proppant mesh injection. All the simulations correspond to the early stage, before the "traction carpet" effect comes into play.

© 2018 Elsevier Ltd. All rights reserved.

1. Introduction

Conventional and unconventional oil and gas production is often stimulated by means of hydraulic fracturing. This technique consists in injecting fluids at high pressure into the wellbore to induce fractures in the formation that later serve as highly conductive paths. To avoid fracture closure after hydraulic pressure release, the fracturing fluids contain granular materials (such as selected or treated sand, ceramics, polymeric pellets, etc.) that remain trapped in the formation. Once packed, these granular materials, called proppants, provide a porous media in the fracture through which hydrocarbons can flow (Economides et al., 1989). After pressure release, any unpropped region of the fracture will close and the conductivity of the whole fracture will be dramatically reduced (Zhang et al., 2017b). For that reason, the actual placement and distribution of the proppant in the fracture is one of the critical factors that determines the subsequent production of

the well. Despite hydraulic stimulation has been used since 1950, many question on proppant transport and placement in fractures remain unanswered (Bokane et al., 2013). Other factors that have an impact on productivity are the proppant crushing resistance and proppant pack stability during production.

When gelling agents are used in fracturing fluids, proppant particles remain in suspension until fracture closure, upon pressure release. However, when low viscosity fluids are used (slickwater), the proppant rapidly settles forming a dune at the bottom of the fracture (Mack et al., 2014). Due to its lower cost, limited reservoir damage and good performance on subsidiary fractures, slickwater is widely used to economically develop unconventional resources (Alotaibi et al., 2015; Palisch et al., 2010). It is worth mentioning that the transport capabilities of such thin fluids are very limited, and also the transport mechanisms are different from those observed in gels (Palisch et al., 2010).

A pioneer experimental work on a laboratory scaled vertical fracture (Kern et al., 1959) has shown that during proppant injection, using slickwater, a dune develops. At very high pumping rates, the sand can be fully washed out, however, at moderate flow rates the dune grows in height. This reduces the gap between the tip of the dune and the ceiling of the fracture, which increases the

---

* Corresponding author at: Dpto. Ing. Mecánica, Universidad Tecnológica Nacional, Facultad Regional de La Plata, CONICET, Av. 60 Esq. 124, La Plata, 1900, Argentina.

E-mail addresses: mbaldini@frlp.utn.edu.ar (M. Baldini), luis.pugnaloni@frlp.utn.edu.ar (L.A. Pugnaloni).

fluid velocity within this gap for a constant flow rate. As a result, the sand is dragged downstream deep into the fracture and the dune grows in width, being the proppant transport dominated by saltation and creep (Mack et al., 2014). Eventually, an equilibrium dune height is established at this point and a "traction carpet" develops where sand is transported in a narrow layer on top of the dune (Kern et al., 1959). Other authors reported similar results (Patankar et al., 2002; Sahai et al., 2014; Wang et al., 2003; Woodworth et al., 2007) agreeing that proppant injected after the "traction carpet" overshoots the initial sediment bank and is dragged further into the fracture. In spite of this, Medlin et al. (1985) argue that in a real fracture this "traction carpet" effect can rarely be achieved.

Numerical simulations are also widely used to predict proppant transport and determine its distribution in the fractures. There are mainly two groups of methods to solve this type of multiphase flow: the Eulerian–Eulerian and the Eulerian–Lagrangian approaches. In the Eulerian–Eulerian methods, both the fluid and the solid phase are resolved using Eulerian grids. Two popular methods are the Two Fluid Model (TFM) (Anderson and Jackson, 1967) and the concentration model (Settari et al., 1984). The TFM considers the solid and the fluid phases as two interpenetrating fluids coupled via momentum exchange. The biggest challenge of this type of approach is to define the constitutive equations for the solid phase (Zhou et al., 2010). In the concentration method, the transport of the solid phase is described through a scalar field (concentration). Dontsov and Peirce (2014, 2015) presented a model that includes gravitational settling and polydispersity, and obtained a distribution of proppant in a fracture. Generally speaking, the Eulerian–Eulerian approaches require small computational resources due to the fact that the particles are treated as an averaged continuum and details of the particle–particle interaction are ignored. In slurry flows, the particle–particle interactions become important; hence, a micromechanical description is valuable. In the Eulerian–Lagrangian methods the fluid phase is resolved in a Eulerian grid and the solid phase is resolved in a Lagrangian fashion, solving the Newton equations for each solid particle. Detailed information at the particle level can be obtained using this schemes. Two popular methods are the MP–PIC (Multi Phase–Particle in Cell) (Snider, 2001) and the CFD–DEM (Computational Fluid Dynamics–Discrete Element Method) (Zhou et al., 2010; Tsuji et al., 1993; Xu and Yu, 1997). Patankar and Joseph (2001) first introduced the MP–PIC method to study proppant transport. Tsai et al. (2012) used the MP–PIC to investigate the effects of different parameters in proppant transport.

In recent years, the CFD–DEM method has gained popularity to model proppant transport due to the detailed information on particle positions, velocities and interacting forces (Tsuji et al., 1993). Nevertheless, as it requires larger computational resources, small scaled systems are generally modeled (Basu et al., 2015). Zhang et al. used this method to model proppant distribution in horizontal wells (Zhang et al., 2017c). They found that big proppant particles tend to settle quickly near the wellbore while lighter proppant particles can be transported a longer distance into the fracture. If proppant is injected at a low rate, it settles close to the wellbore and the transport distance is short. They also obtained more spread dunes by moving the injection point from a lower to an upper position. In another work, Zhang et al., considered micromechanic effects on proppant transport during hydraulic fracturing (Zhang et al., 2017a). They found that the dune shape can be affected if a significantly low particle stiffness is used, this is due to the fact that the allowed shear force is consequently small. The particle–particle friction coefficient has also an effect on the dune shape and repose angle, a low particle–particle friction coefficient leads to a secondary dune formed by particle avalanches. Tomac et al. also studied the micromechanics of proppant transport in a narrow hydraulic fracture (Tomac et al., 2013) including a fluid lubrication model to reproduce effects such as proppant pack formation and clogging. They found that high particle concentrations induce to more frequent particle–particle interactions and, as a consequence, the fluid lubrication effect becomes important, leading to an increase of particle agglomeration. This effect is more pronounced in high viscosity fluids and under low fluid drag conditions. They also showed that these agglomerations difficult the prediction of transport in terms of channel pressure drop for high particle concentration. Zhang et al. also analyzed the transport of multisized proppant in vertical wells (Zhang et al., 2017b). They described the three stages of proppant transport: *dune formation* governed by settlement and fluid drag, *dune development* governed by fluidization and *bank formation* governed by erosion due to the high velocity of the "traction carpet". Blyton et al. (2015) used the CFD–DEM method to adjust a commercial fully 3D hydraulic fracturing simulation via correlations, they found that the proppant average velocity is generally lower than the fluid phase velocity and that the settling velocity of proppant can be higher or lower than the one predicted by the Stoke's law, with additional dependencies on relative size of proppant to slot width, proppant concentration, and Reynold's number. If an upscaling technique is applied, CFD–DEM can be also used to model real scale fractures as can be seen in the work by Zeng et al. (2016). The "traction carpet" effect, initially described by Kern et al. (1959), was observed in CFD–DEM simulations by several authors (Tong and Mohanty, 2016; Zhang et al., 2017b; 2017c; 2017a; Zeng et al., 2016).

In this work, we consider the placement of proppant during the injection process by modeling a vertical planar fracture and its filling by a Newtonian fluid that transports spherical grains. Most studies of this type consider the proppant injection though one inlet on one side of the narrow cell used to model the fracture (Zhang et al., 2017c; 2017a) or, alternatively, using a homogeneous injection all along the height of the cell on the wellbore side (Zhang et al., 2017b; Zeng et al., 2016). In contrast, we inject fluid at four inlets to try to emulate four perforation clusters. We measure the effect of placing the perforation clusters at different heights in the well by measuring the dune profile for three different positions. Instead of considering the continuous deposition of sand in the dune during a long period of time, we focus on the initial stages, when a significant dune forms after a short pumping period but before a fully developed traction carpet is observed.

The initial phase of injection is an important aspect of the entire stimulation process. In particular, the initial injection is considered critical for propping the far field. A number of technologies are based on the expected flow during this stage. An example of this is the choice of light density proppants and fine meshes to improve the initial transport in the fluid phase before any significant settlement occurs. We show that the positioning of the injection clusters has an impact on the early stage dune which modifies the flow pattern and affect the subsequent proppant placement.

We also consider the distribution of proppant when two different granular materials are pumped into the fracture. Grains of different density are injected in different orders. The final shape and position, as well as the degree of mixing, is very sensitive to the injection strategy (either changing the inlets position or the order of proppant injection). We measure the degree of mixing quantitatively by using the concept of mixing entropy (Wen et al., 2015). This tool allows a much more detailed analysis on mixed systems than previously observed in proppant placement studies.

It is worth mentioning that the model cell, injection points, and flow rates have been scaled taking as a reference a field fracture (Ortiz et al., 2016). During this scaling, the flow rates required in the model have been found to be somewhat higher than in previous studies. This allows a relatively realistic extrapolation to field scales, usually difficult to carry out in previous works.
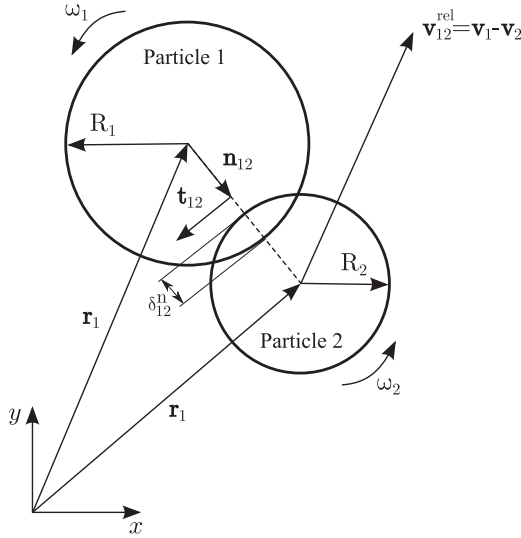
Fig. 1. Contact model between two spherical particles of radii R_1 and R_2. $\mathbf{r_1}$ and $\mathbf{r_2}$ are the position vector of particles and ω_1 and ω_2 the colliding particles angular velocities. δ_{12}^n is the overlap between particles and $\mathbf{v}_{12}^{rel}$ the relative velocity between particles.

2. CFD–DEM modeling

We carried out our simulations by using a CFD–DEM approach, coupling the fluid and solid phase through momentum exchange. The fluid phase is solved using the Finite Volume Method (Versteeg and Malalasekera, 2007) and the granular with the Discrete Element Method (DEM) (Pöschel and Schwager, 2005). The implementation used is the one provided by CFDEM® (Goniva et al., 2012), which couples LIGGGTHS®[1] (Kloss et al., 2012) for the solid phase and OpenFoam[2] for the fluid phase.

2.1. DEM

Each proppant particle is modeled as a soft sphere, and the motion of each particle is calculated by solving the Newton–Euler equations of motion for a rigid body (Pöschel and Schwager, 2005), which are then integrated over time to calculate particle trajectories.

$$m_i \frac{d^2 \mathbf{r}_i}{dt^2} = \mathbf{F}_i^n + \mathbf{F}_i^t + \mathbf{F}_i^f + \mathbf{F}_i^b,$$
$$I_i \frac{d\boldsymbol{\omega}_i}{dt} = \mathbf{r}_{i,c} \times \mathbf{F}_i^t, \qquad (1)$$

where $\mathbf{F}_i^n$ and $\mathbf{F}_i^t$ are the resultant forces of the normal and tangential contributions for every particle–particle and particle–wall contact over the particle i. The force exerted by the fluid phase on the particles $\mathbf{F}_i^f$ is generally expressed as $\mathbf{F}_i^f = \mathbf{F}_i^d + \mathbf{F}_i^p + \mathbf{F}_i^v$, where $\mathbf{F}_i^d$ is the drag force, $\mathbf{F}_i^p$ is the pressure force and $\mathbf{F}_i^v$ the viscous force acting on the particles. Any other external force such as gravitational, electromagnetic, etc., is taken into account by $\mathbf{F}_i^b$. m_i and I_i are the mass and moment of inertia of the particle i.

Two particles i and j with radius R_i and R_j, at positions r_i and r_j (see Fig. 1) are in contact if $\delta^n = R_i + R_j - |\mathbf{r_i} - \mathbf{r_j}| > 0$ and interact with a force which is expressed in terms of the normal and

tangential components (Pöschel and Schwager, 2005),

$$\mathbf{F}_{ij} = F_{ij}^n \mathbf{n}_{ij} + F_{ij}^t \mathbf{t}_{ij}, \qquad (2)$$

being $\mathbf{n}_{ij} = |\mathbf{r_i} - \mathbf{r_j}|/(\mathbf{r_i} - \mathbf{r_j})$ and $\mathbf{t}_{ij}$ the normal and tangential unit vectors. There are several models to describe the contact forces in DEM simulations, suitable for different particle geometry and material behavior (Pöschel and Schwager, 2005; Shäfer et al., 1996; Kruggel-Emden et al., 2007; 2008; Brilliantov et al., 1996). Assuming a Herzt contact force (Hertz, 1882) and a dissipative force (Tsuji et al., 1993; Hu et al., 2010), the normal component is given by

$$F_{ij}^n = k^n (\delta^n)^{3/2} + \gamma^n (\delta^n)^{1/4} \dot{\delta}^n, \qquad (3)$$

where δ_n is the normal overlap and $k^n = \frac{4}{3} E^* \sqrt{R^*}$ accounts for the material elastic properties (Pöschel and Schwager, 2005). The dissipative interaction constant (γ^n) results from the solution of the Herztian spring-dashpot model (Antypov and Elliott, 2011) $\gamma^n = -2\sqrt{\frac{5}{3} E^* m^* (R^*)^{1/4}} \frac{\ln e}{\sqrt{\ln e^2 + \pi^2}}$. The expression for γ^n considers a velocity independent coeficcient of restitution e (Tsuji et al., 1993). The effective Young's modulus E^*, radius R^*, and mass are defined as (see Di Renzo and Di Maio, 2005) $1/E^* = (1 - \nu_1^2)/E_1 + (1 - \nu_2^2)/E_2$, $1/R^* = 1/R_1 + 1/R_2$ and $1/m^* = 1/m_1 + 1/m_2$, ν correspond to the Poisson ratio (see Di Renzo and Di Maio, 2005).

In the tangential direction, the interaction follows a modified version of the model by Cundall and Strack (1979), Tsuji et al. (1993) and Hu et al. (2010)

$$F_{ij}^t = -\text{sign}(v_{ij}^t) \min\left(\left|k^t \delta^t (\delta^n)^{1/2} - \gamma^t \dot{\delta}^t (\delta^n)^{1/4}\right|, \mu F_{ij}^n\right), \qquad (4)$$

where $k^t = 8 G^* \sqrt{R^*}$ and $\gamma^t = -4\sqrt{\frac{5}{3} G^* m^* (R^*)^{1/4}} \frac{\ln e}{\sqrt{\ln e^2 + \pi^2}}$ (see Tsuji et al., 1993; Hu et al., 2010; Kloss et al., 2012). G^* is the effective shear modulus given by $1/G^* = (2 - \nu_1)/G_1 + (2 - \nu_2)/G_2$ (see Di Renzo and Di Maio, 2005). The shear modulus can be obtained from the Young's modulus by $2G_i = E_i/(1 + \nu_i)$. F_{ij}^t is limited by Coulomb friction, being μ the friction coefficient. The tangential displacement depends on the history of the contact and is calculated as

$$\delta^t(t) = \int_{t_K}^{t} v_{ij}^t(t') dt, \qquad (5)$$

being t_K the time when the contact first occurs (Pöschel and Schwager, 2005).

The equations of motion for N grains are solved via a velocity-Verlet algorithm by advancing in small time intervals Δt. The LIGGGTHS® implementation for this DEM simulation includes a number of techniques to speedup the simulations, including neighbor lists, parallelization, etc. Since the particles interact with the fluid phase, an additional external force is applied to each grain according to the local properties of the fluid (see Section 2.3).

2.2. CFD

The governing equations for the fluid phase are the so-called Volume Averaged Navier Stokes Equations (VANS) (Norouzi et al., 2016). This set of equations are valid when each fluid cell is large enough to contain a few particles, in that case cell-averaged variables for the fluid phase can be defined. This approach is often referred to as "unresolved" (Kloss et al., 2012; Hager, 2014). The fluid phase mass conservation equation for an incompressible fluid is:

$$\frac{\partial \alpha_f}{\partial t} + \nabla \cdot (\alpha_f \mathbf{u}_f) = 0, \qquad (6)$$

where α_f is the volume fraction of fluid in the computational cell and $\mathbf{u}_f$ is the velocity of the fluid.

The momentum conservation equation for the fluid phase is

$$\frac{\partial (\alpha_f \mathbf{u}_f)}{\partial t} + \nabla \cdot (\alpha_f \mathbf{u}_f \otimes \mathbf{u}_f) = -\alpha_f \nabla \frac{p}{\rho_f} - \mathbf{R}_{pf} + \nabla \cdot (\alpha_f \boldsymbol{\tau}) + \alpha_f \rho_f \mathbf{g},$$

---

[1] Open source discrete element method particle simulation code. http://www.cfdem.com/liggghts-open-source-discrete-element-method-particle-simulation-code .

[2] Open source field operation and manipulation. http://www.openfoam.org .

(7)

where ρ is the fluid density, p is the fluid pressure, $\mathbf{R}_{pf}$ is the momentum exchange between the fluid and the solid phase, τ is the fluid stress tensor and $\mathbf{g}$ is the gravity. To solve the governing equations a pressure-based solver using "Pressure-Implicit Split-Operator" (PISO) pressure–velocity coupling is used (Jasak, 1996; Issa, 1986). The fluid is considered as Newtonian and the k-ϵ turbulence model was adopted (Versteeg and Malalasekera, 2007).

2.3. Coupling

As we already mentioned in Section 2.2, the phase coupling between the fluid and the particles is done through momentum exchange. To calculate the fluid–particle interaction force, a Lagrangian–Eulerian mapping needs to be made. The momentum exchange between phases in a given cell can be modeled as

$$\mathbf{R}_{pf} = K_{pf}(\mathbf{u}_f - \langle \mathbf{v} \rangle), \tag{8}$$

being $\langle \mathbf{v} \rangle$ the average particle velocity in the cell and $\mathbf{u}_f$ the cell fluid velocity. K_{pf} is given by

$$K_{pf} = \frac{\left| \sum \mathbf{F}_i^d \right|}{V_{cell} |\mathbf{u}_f - \langle \mathbf{v} \rangle|}, \tag{9}$$

being $\mathbf{F}_i^d$ the fluid–particle drag force, which needs to be summed for all the particles in the cell of volume V_{cell}. The contributions of the pressure gradient force and the viscous term are already included in the stress tensor τ. See Hager (2014) and Zhou et al. (2010) for more details. There are many available models to calculate the drag force. We use the Di Felice drag correlation (see, Di Felice, 1994; Zhu et al., 2007) in which the drag force on a given particle i is determined through

$$\mathbf{F}_i^d = \frac{1}{2} \rho_f (\mathbf{u}_f - \mathbf{v}_i) |\mathbf{u}_f - \mathbf{v}_i| C_d \frac{\pi d_p^2}{4} \alpha_f^{(2-\beta)}, \tag{10}$$

being $\mathbf{v}_i$ the velocity of particle i, C_d the particle drag coefficient and β a model coefficient

$$C_d = \left(0.63 + \frac{4.8}{\sqrt{Re_p}} \right)^2,$$

$$\beta = 3.7 - 0.65 \exp\left[-\frac{(1.5 - \log Re_p)^2}{2} \right]. \tag{11}$$

Re_p is the particle Reynold's number

$$Re_p = \frac{\rho_f d_p \alpha_f |\mathbf{u}_f - \mathbf{u}_p|}{\mu_f}, \tag{12}$$

being μ_f the fluid viscosity.

3. Numerical test

To test our numerical scheme, we have carried out a simulation to reproduce the results reported in Zhang et al. (2017a). Despite most of the simulation parameters are specified in that paper, some values had to be estimated. The simulation domain consists in a "two-dimensional" cell (the domain has a thickness of one particle diameter) with a length of 0.3 m and a height of 0.09 m. A fluid with a density $\rho_f = 1000$ kg/m^3 and a viscosity $\mu_f = 10^{-2}$ Pa·s is injected at 0.5 m/s though one inlet at mid height on the left side. The dimension of the inlet is not clearly specified in Zhang et al. (2017a), but it is mentioned that it is of the order of three particle diameters. The particles have a diameter of 1 mm and a density $\rho_p = 3200$ kg/m^3. To mimic the particle stiffness used by Zhang et al. in their linear spring model, we had to estimated our Young's modulus in the Hertz model by fitting the non-linear behavior with a linear law in a reasonable range of

overlaps expected. We used $E = 1.7 \times 10^7$ Pa. The restitution coefficient was set to $e = 0.5$ and the Poisson ratio to $\nu = 0.5$. Several particle–particle and particle–wall friction coefficients where tested by Zhang et al.; however, we have chosen to put our focus on the results for $\mu_w = \mu_p = 0.65$ because this case is reported more comprehensively. Neither the particle rate nor the total number of particles injected are reported, so these parameters had to be estimated from the images in Zhang et al. (2017a). We do this by noting that after 35 s of their simulation, roughly 60% of the cell is filled with particles. To achieve this, a particle rate of about 366 particles/s had to be used in our simulations.

In Fig. 2, we compare our results with those reported by Zhang et al. To do this, we have plotted on top of our snapshots the profile of the dune of particles extracted from Zhang et al. (2017a). It is clear that the results agree not only qualitatively but also quantitatively. In Fig. 2 we see that, when the particles are injected in the cell, a large anti-clockwise eddy is developed and that the particles tend to settle close to the injection point. We see that at this early stage a dune starts to form. Later, this dune grows. We see that the dune shape at $t = 3$ s is somewhat smaller than the dune reported by Zhang et al., but it has a similar shape. At $t = 13$ s, the dune becomes of such height that the gap between the dune and the top of the cell narrows significantly. As a consequence, the fluid velocity grows within this gap and is able to carry the incoming particles above the dune. This effect is called "traction carpet" and was reported several times in the literature. For $t = 25$ s the traction carpet has become the predominant driver of the particle transport and the dune length has reached 0.177 m, in fair agreement with Zhang et al. Finally, at $t = 35$ s, we show the repose angle observed, in our simulation $\theta = 47°$ and Zhang has reported a repose angle of $\theta = 41°$. Despite the subtle differences in the results, and considering that some parameters of the simulations had to be estimated, the agreement with the literature suggest that our simulations are consistent with others.

4. Numerical model

4.1. Model scaling

In order to mimic the proppant transport in a real fracture, we have made an effort to scale down a reference field fracture warranting kinematic and dynamical similitude as much as possible. The scaling of these type of experiments has been discussed previously by others (Sahai et al., 2014).

As a reference, we consider a planar vertical fracture (half-wing) in a very low permeability formation (e.g., a shale) having 6.0 mm in thickness, 80.0 m in length and 40.0 m in height. We assume the fracturing fluid is pumped at a constant flow rate of 0.1 m^3/s (i.e., ≈ 40 bpm) which is divided in half to feed each half-wing. Therefore, the mean fluid velocity in the fracture is 0.21 m/s. We also assume that injection is made through four perforation clusters (along a vertical wellbore), each having an effective cross section of 1500 mm^2. In practice, each perforation cluster consist in a number of perforations (1500 mm^2 would correspond to 30 perforations of 8 mm in diameter) that in our model we will represent by a single effective perforation.

The particle Reynolds number in a Newtonian fluid is defined as $Re_{part} = \rho v d/\mu$, where ρ is the fluid density, d is the particle diameter and v its velocity with respect to the fluid. The proppant particles in our model have the same size as those used in field operations, and the conveying fluid has also the same density and viscosity. Therefore, to achieve the same Re_{part} as in the field, the model simply needs to use the same fluid velocity v. For this, the flow rate in the model has to be set to a value that warrants that the mean velocity of the fluid in the cell is the same as in the
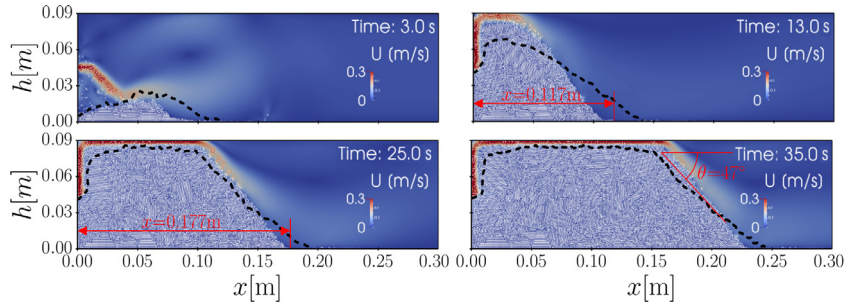
Fig. 2. Snapshots of the simulations for a system under the conditions studied in Zhang et al. (2017a). The color scale corresponds to the fluid velocity modulus in m/s. The white dots correspond to the proppant particles. The dotted lines correspond to the profile of the dune of particles extracted from the images of Zhang et al. (For interpretation of the references to color in this figure legend, the reader is referred to the web version of this article.).

field (i.e., 0.21 m/s). This is consistent with previous estimations (Sahai et al., 2014).

The Reynolds number for any perforation cluster, considered as a pipe, is defined as $Re_{perf} = \rho v d_{perf}/\mu$, for a Newtonian fluid, with d_{perf} the diameter of the perforation and v the velocity of the fluid. Hence, to achieve a comparable Reynolds number, the model must conserve the product $v d_{perf}$. For our field reference perforation clusters (1500 mm^2 in cross section) and flow rate (0.1 m^3/s through two half wings and four clusters each), the fluid velocity in each perforation is ≈ 8.0 m/s.

It is important to emphasize that most previous simulation studies consider flow velocities (at the perforations) which are significantly smaller than these values suggested by the scaling. Injection velocities of 0.15–0.5 m/s in each inlet are typically used (Zhang et al., 2017a; 2017c; 2017b). Likewise, some studies do not consider injection points but a homogeneous injection along the height of the fracture (Basu et al., 2015; Tong and Mohanty, 2016), disregarding the complex flow pattern induced by a more realistic localized injection.

Our numerical model fracture is scaled 1:50 in the horizontal and vertical directions with respect to the reference fracture. Therefore the flow rate will be 100 times smaller than in the field to conserve the mean fluid velocity. We recall that only one half-wing of the fracture is simulated. This warrants that the Reynolds numbers are equivalent to the ones in the field and that the field fracture and the model are kinetically similar; i.e., the ratio between the fluid velocity in two corresponding points (field and model) is always the same. In our case, this ratio is 1 (one). As a consequence, the time scales ([T] = [L]/[V]) are reduced 50 times with respect to the field operation. In practice, this means that a full operation that takes 100 min in the field will be accomplished in 2 min in the model. The simulations discussed in this work are of about 15 s, which are equivalent to about 13 min of a field operation.

4.2. Model definitions

We model a vertical planar fracture as a vertical slot 800 mm height and 1600 mm long (see Fig. 3). This corresponds to 1/50 of the linear dimensions of the reference field fracture described above. The cell has a thickness 1.5 times the particle diameter (d_p) to avoid high packing fraction due to particle ordering. Although wider fractures are also observed in hydraulic treatments, depending on the geomechanical properties of the formation and the fracturing fluids, narrow fractures are also observed. One might expect that such narrow fractures may screenout easily. However, Barree et al. (2001) have shown that slots usually do not create stable proppant bridges even at very narrow apertures as the one simulated here. The slot has four injection points on the left side, whose centers are separated by 73 mm. Each injection point is a
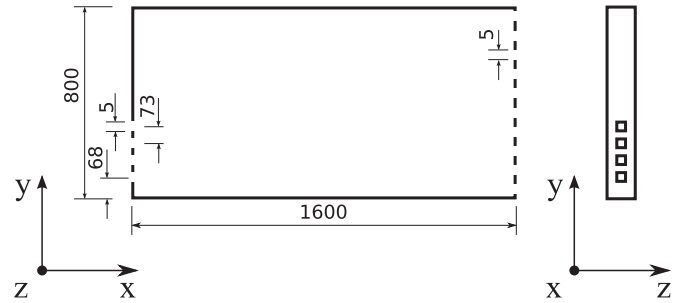

Fig. 3. Sketch of the front and side view of the simulation slot (not to scale). Distances are measured in mm. The slot has a thickness of 1.5d_p in the z-direction. Only one (bottom) of the three alternative positions used for the inlet cluster (perforations on the left) is shown.

rectangular area 5 mm height and 1.35 d_p wide. The injection cluster can be positioned at three different alternative heights along the inlet side of the slot: (bottom) 68 mm, (middle) 287 mm, and (top) 508 mm from the base of the cell to the lowest injection point. On the right side, ten outlets, having the same dimension as the inlets, allow the fluid (but not the particles) to exit. At the inlets, a prescribed fluid velocity and a null pressure gradient in the x-direction are imposed. At the outlets, the outside pressure is set to zero and the velocity gradient is null in the x-direction. The perimeter of the slot (apart from the inlet and outlet orifices) has a no slip boundary condition. The front and back planes have symmetric boundary conditions.

The fluid phase has a density of $\rho_f = 1000$ kg/m^3 and a viscosity of $\mu_f = 1$ cP (Newtonian fluid). The domain is discretized using hexahedric cells with two levels of detail: a coarse mesh with 48,960 cells, and fine mesh with 195,840 cells. The refined mesh was obtained from the original mesh by splitting each cell in 4 smaller cells. The coarse mesh is used in most simulations and the fine mesh is used only to validate the results. The time steps for the CFD calculation where 1×10^{-4} s and 2.5×10^{-4} s depending on the mesh. The selected time steps satisfy the Courant–Friedrichs–Lewy (CFL) condition in order to maintain numerical stability (Hirsch, 2007). For the one dimensional case, the CFL condition is defined as $CFL = \frac{v \Delta t}{\Delta x}$, where v is the fluid velocity, Δt is the time step and Δx is the mesh size. Following other authors recommendations, it is advisable to keep CFL below 0.5 to obtain accurate results (Mondal et al., 2016). The CFD time step it is also bounded by the coupling interval, which in our case is of 50 DEM time steps. The time step for the DEM calculation was 5×10^{-5} s to achieve acceptable values of the Raleight and Hertz time. The Raleight critical time step can be determined though the expression given in Li et al. (2005): $\Delta t_R = \frac{\pi R^*}{0.8766 + 0.163\nu} \sqrt{\frac{\rho}{G}}$. There is not an analytical expression to calculate the Hertz time, but it can

be estimated during runtime to check if the time step is appropriate using the expression $\Delta t_{\mathrm{H}} = 2.87 \left(\frac{m^*}{R^* E^* V_{\max}} \right)$, being $V_{\max}$ the maximum collisional velocity observed. It is recommended to pick a DEM time step not bigger that 10% of the Raleight and Hertz time to properly model particle–particle and particle–wall interaction (Washino et al., 2016). The chosen value was kept constant in all simulations.

Four different types of particles were considered: particles of two different diameters (0.6 and 0.8 mm) and two densities (2600 kg/m³ and 3600 kg/m³). These diameters correspond to the mean diameter of two mesh sizes, 20/40 (0.6 mm) and 16/30 (0.8 mm) respectively. The chosen densities correspond to typical values for sand (2600 kg/m³) and ceramic (3600 kg/m³). The different proppants used are then 20/40 sand, 16/30 sand, 20/40 ceramic and 16/30 ceramic. The contact parameters k^{n}, γ^{n}, k^{t} and γ^{t} were determined from the mechanical properties of both materials as we stated in Section 2.1. Due to the fact that the fluid dominates the system dynamics, we have chosen average contact properties for both materials (Young's modulus E $= 5 \times 10^6$ Pa, Poisson's ratio $\nu = 0.5$, restitution coefficient $e = 0.7$ and friction coefficient $\mu = 0.5$).

The Young's modulus selected is lower than the actual values for sand and ceramic. This is to achieve a reasonable DEM time step and reduce CPU time. It has been shown that this practice has no significant impact on DEM simulations (Ertaş et al., 2001). The interaction with domain boundaries is characterized by the same contact parameters as the particle–particle interaction.

We carry out four simulations for each injection cluster position (bottom, middle and top): one for each possible combination of mesh size and material (sand 16/30, sand 20/40, ceramic 16/30 and ceramic 20/40). At the inlets, the fluid is injected by increasing the velocity linearly from 0 to 8 m/s in 1 s. Then, during 4 s, the fluid injection is kept at 8 m/s while 3×10^5 proppant particles are injected by creating particles in front of each inlet at a prescribed rate (i.e., 18750 particles/s in front of each perforation). Finally, the injected fluid velocity is reduced to 0 m/s in 1 s. The simulation is let to run long enough after the fluid injection has ceased so that the proppant grains are able to settle in the slot. This takes around 10 s, depending on the proppant type and the injection cluster position. The average volume occupied by the larger particles in the slot is about 77% larger than the volume occupied by the smaller particles, because although the cell thickness is scaled with the particle diameter ($1.5 \times d_{\mathrm{p}}$) the occupied volume ratio goes with r_1^2/r_2^2, being r_1 and r_2 the particle radii for each mesh size.

Three additional simulations were done by injecting the two types of proppant of the same mesh, but different material, one after the other and also simultaneously as a mixture. In one simulation, ceramic proppant is injected after all sand proppant has been introduced and in another simulation sand is injected only after ceramic proppant has been injected. In a final simulation both proppant types are injected simultaneously. In any given simulation 1.5×10^5 grains of each type are injected at the same rate.

Fluid mesh independence has been tested comparing simulations with a coarse and a fine fluid mesh. To this end, we have focused on the overall velocity field and the final dune profile for the middle injection position. Also a domain-dependence analysis was done by extending 50% the domain length. Also here, the overall flow field and the dune profile were analyzed (see Section 5.1).

5. Results

5.1. Numerical model sensitivity analysis

In order to check if the CFD mesh size is suitable, we have performed a sensitivity analysis of the numerical model. Two CFD mesh sizes where tested as described in Section 4. The results

were compared by plotting the final dune profile after settlement. The profile of each dune is extracted from the particle coordinates after settling. We have divided the cell length into small vertical bins (1.00 cm wide) for which we have calculated the vertical coordinate of the center of mass (z_{CM}), taking into account the particles whose centers are inside the bin. By assuming that the packing fraction is roughly constant along the column of particles, the position of the free surface ($h(x)$) at a given bin is estimated as $h(x) = 2z_{\mathrm{CM}}$. The assumption of constant packing fraction along the bin holds within 1% of error.

In Fig. 4(a), we can see the final dune for two simulations using 16/30 sand injected through the middle injection position with the coarse and the fine CFD meshes. It is clear that the final dune profiles obtained in both simulations are very similar, and that a fine CFD mesh is not required for the purpose of our study. We have not observed qualitative nor quantitative differences in the flow patterns between the coarse and fine CFD mesh simulations, suggesting again that the results obtained are mesh independent.

Due to the fact that particles are not allowed to exit the simulation domain, we have carried out simulations using a longer cell (2.4 m instead of 1.6 m) to evaluate the effect of domain extension on proppant placement. In Fig. 4(b), we show the final settled dune for 16/30 sand obtained with the same configuration as in Section 5.2 except from the cell length. We can see that using a longer slot yields very similar dunes. This indicates that the shape of the deposited dune is fairly insensitive to the slot length beyond 1.6 m.

The restitution coefficient $e = 0.7$ that we selected for our simulations is similar to those used by other authors. Tsuji et al. (1993) and Xu and Yu (1997) used $e = 0.9$, but Zeng et al. (2016) used $e = 0.5$. Experimentally, Mack et al. (2014) have measured the restitution coefficient of different proppant particles in dry and submerged conditions; showing significant reductions of e when particles are immersed in a fluid. We choose a representative value for both materials studied under dry conditions. However, after running some test simulations with different restitution coefficients, we found that this detail of the particle–particle interaction has very little impact on the geometry of the final dune (see Fig. 4(c)).

5.2. Positioning of the injection cluster

In Fig. 5, we show different snapshots of the simulations of 16/30 sand for the three alternative positions of the injection cluster. Although our cell is larger and our injection velocity is significantly higher, the flow dynamics and the particle transport are consistent with those reported by Zhang et al. (2017a); at least at the initial stage when a considerable proppant dune has been formed. During this initial stage, we see in Fig. 5 that the proppant transport is mainly governed by settlement and fluid drag. This phenomenon has been already reported in another work by Zhang et al. (2017b). Our simulation results shown in Fig. 5 are also in line with the experimental results by Liu (2006). Although Liu's cell doubles our cell length and the injection velocity used is really low, the settled dune and the flow dynamics qualitatively agree. We need to mention that we do not depict the development of a dual dune at the initial stage as is showed in Zhang et al. (2017a). This difference is probably due to the fact that we use four injection clusters instead only one. This changes how the main transport stream is built. In our case, the four injection points produces a wider and more spread transport stream which induces a more homogeneous dune. The bottom injection (left column) leads to a rather small anti-clock-wise transport eddy. Particles initially tend to settle in a sort of triangular-shaped dune close to the injection points. At a later stage, proppant is deposited deeper into the cell. The tip of the dune is finally positioned within the first half of
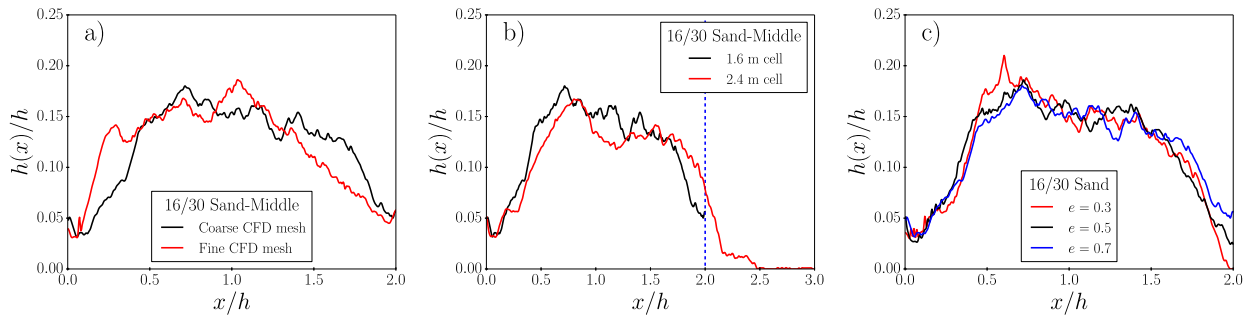
Fig. 4. (a) Final dune profile obtained with the refined CFD mesh (red) case for 16/30 sand for the middle injection compared with the result for the coarse CFD mesh (black). (b) Results obtained for 16/30 sand for middle injection using a cell 2.4 m long (red) compared with the results obtained using a cell 1.6 m long (black). The vertical dotted blue line indicates the boundary for the 1.6 m cell. (c) Final dune profile for 16/30 sand for middle injection using three different restitution coefficients. Lengths are scaled with the height $h = 0.8$ m of the cell. (For interpretation of the references to color in this figure legend, the reader is referred to the web version of this article.)
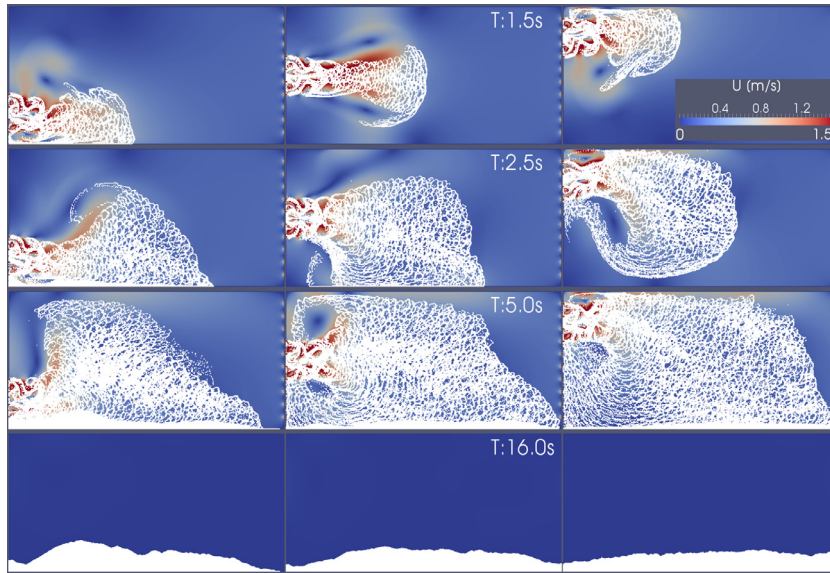

Fig. 5. Snapshots of the simulations for low (left column), middle (middle column) and top (right column) injection cluster at different times during the injection and settlement of 16/30 sand. Each row of images correspond to a given time as indicated in the central column images. The color scale corresponds to the fluid velocity modulus in m/s. The white dots correspond to the proppant particles. (For interpretation of the references to color in this figure legend, the reader is referred to the web version of this article.)
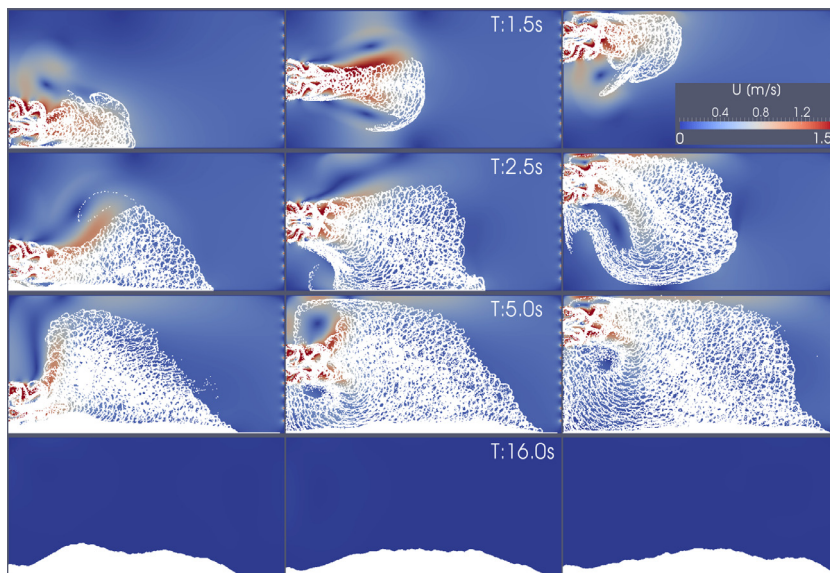

Fig. 6. Snapshots of the simulations for top (right column), middle (middle column) and bottom (left column) injection cluster at different times during the injection and settlement of 16/30 ceramic. Each row of images correspond to a given time as indicated in the central column images. The color scale corresponds to the fluid velocity modulus in m/s. The white dots correspond to the proppant particles. (For interpretation of the references to color in this figure legend, the reader is referred to the web version of this article.)
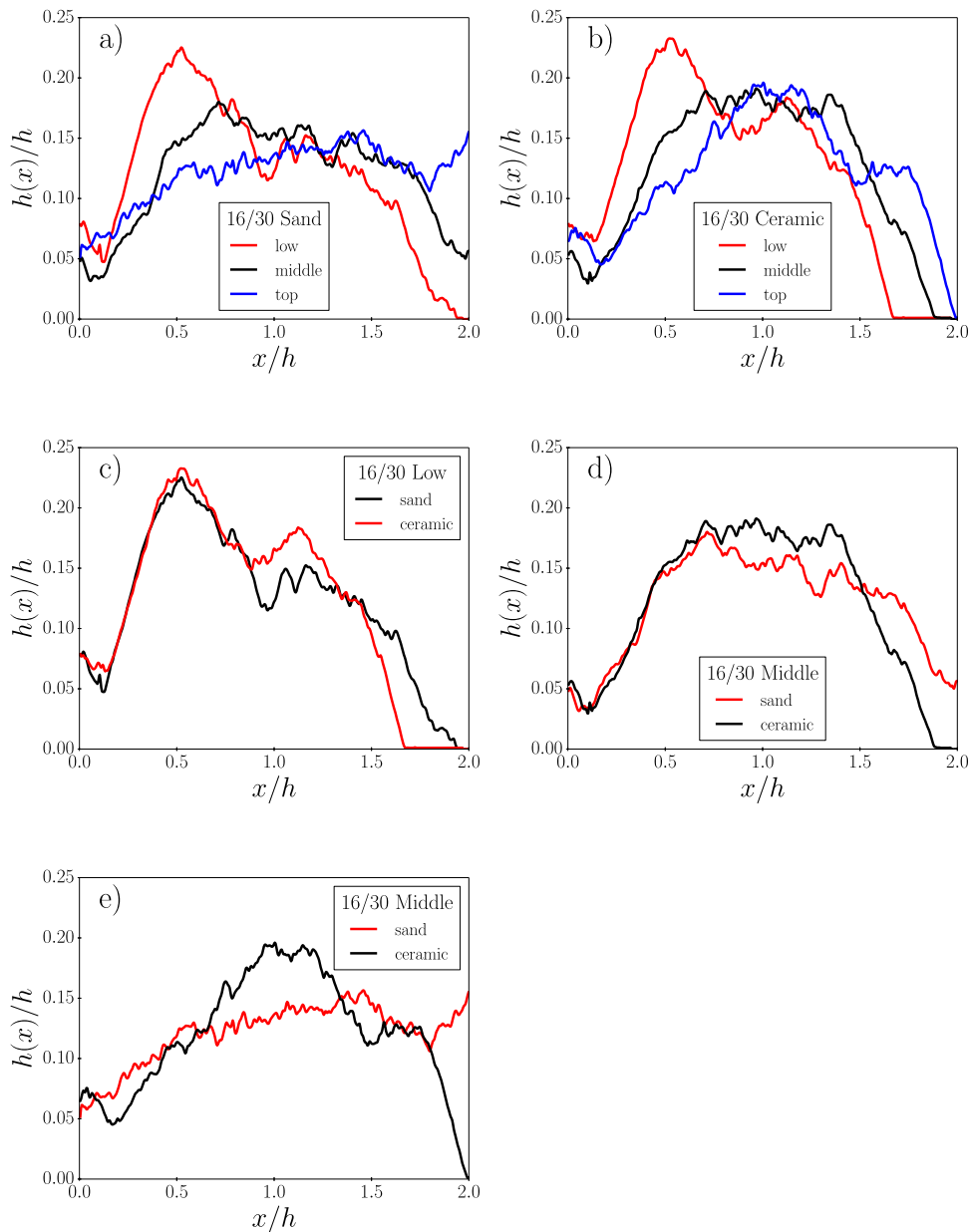
Fig. 7. Dune profiles for the two 16/30 proppant materials using the three injection cluster positions. (a)–(b) Dune profiles for 16/30 sand and ceramic obtained for the three injection positions: low (red), meddle (black) and top (blue) injection. These profiles correspond to the snapshots shown in Figs. 5 and 6. (c) Comparison between sand and ceramic for the low injection. (d)–(e) Same as (c) for middle and top injection, respectively. Lengths are scaled with the height $h = 0.8$ m of the cell. (For interpretation of the references to color in this figure legend, the reader is referred to the web version of this article.)

the cell. The middle injection creates a central stream of particles that leads to a more homogeneous spread of the proppant across the cell length (middle column). The top injection induces a large clock-wise transport eddy also leading to a homogeneous settlement along the cell (right column). These results are in line with those by Zhang et al. (2017c). They reported that a lower injection point produces a dune closer to the wellbore, while an upper injection leads to a more spread dune that sits further into the fracture.

In Fig. 6, we show the results for 16/30 ceramic proppant. We see a similar particle transport dynamics as in Fig. 5. However, since ceramic is denser than sand, particles settle faster. As it may be expected, for all the positions of the injection cluster, the dune settles closer to the injection points and do not reach the right end of the cell in the case of ceramic. These results are consistent with those by Zhang et al. (2017c). They reported that bigger (or heavier) proppant particles yield a dune closer to the wellbore at the

initial stage. In contrast, lighter or smaller particles can be dragged further into the fracture. Similar results have been shown experimentally by Sahai et al. (2014). These authors injected different sand mesh sizes into a slot and noticed that the bigger sand grains settled near the entrance and the smaller grains where carried beyond the experimental device by the outflow.

To compare results quantitatively, we measured the final dune profiles. In Fig. 7(a) we can see the final dune profile for 16/30 sand for the three positioning of the injection cluster. It is clear from these curves that the low injection produces a dune close to the injection points and the middle and top injections generate a homogeneous deposition of proppant along the cell. In Fig. 7(b) we see the same profiles for 16/30 ceramic. As we already saw in Fig. 6 the low injection produces, also for ceramic, a dune closer to the injection points than the middle and top injections.
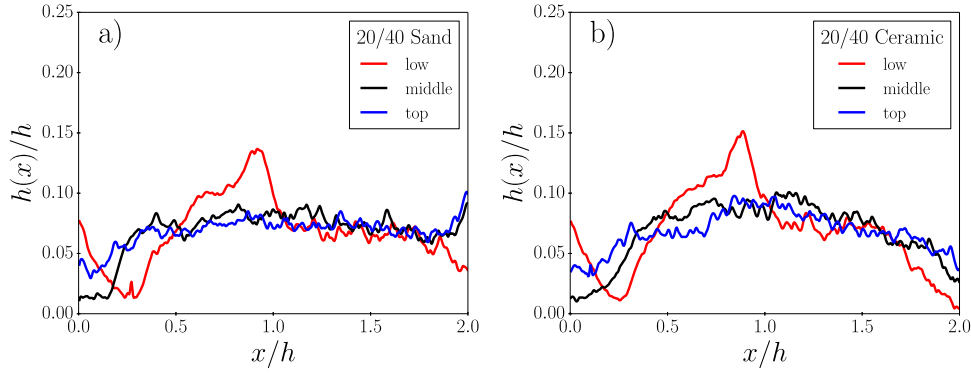
Fig. 8. Dune profiles for sand and ceramic for the three injection cluster positions for mesh 20/40: low (red), meddle (black) and top (blue) injection. Lengths are scaled with the height $h = 0.8$ m of the cell. (For interpretation of the references to colour in this figure legend, the reader is referred to the web version of this article.)

In Fig. 7(c)–(e), we see the effect of proppant density on the final dune profile. We see that in all cases increasing proppant density results in a dune placed nearer the cell entrance; however, this effect is rather subtle.

Finally, we repeated the simulation of the three injection points for both materials using the finer proppant of 20/40 mesh ($d_p = 0.6$ mm), the dune profiles can be seen in Fig. 8. We see that for both cases, sand and ceramic, only the low injection produces a clear tip in the dune. The middle and top injections yield, for both materials, a rather flat layer of particles at the bottom of the cell.

5.3. Injection order strategy

The effect of injecting sand or ceramic proppant of size 16/30 in different orders for a middle injection cluster position can be seen in the snapshots of Fig. 9. Injecting both proppant types simultaneously leads to a homogeneous mix of particles across the cell. Injecting ceramic first leads to a layer of ceramic at the bottom of the cell on top of which a layer of sand is deposited. Injecting sand first (a usual field practice) leads to the opposite situation, a very spread distribution of sand at the bottom of the slot (consistent with the results of Section 5.2) on top of which the ceramic particles settle down. We can see that, due to the lower density, sand can be dragged further into the cell creating a larger deposit at the right end (compare ceramic and sand areas in the middle and right column of Fig. 9 at 16 s). Due to the flow dynamics, the particles that remain in suspension and need more time to settle create a second layer of material on top of the original dune (ceramic or sand) (see middle and right column of Fig. 9 at 16 s).

From Fig. 10 we see that the overall dune profile obtained using the different injection protocols (simultaneous, ceramic–sand and sand–ceramic) is fairly similar. The most significant difference is found when sand is injected before ceramic. In this case sand is placed a bit deeper into the fracture. We can say that under these conditions, changing the injection protocol only modifies the proppant degree of mixing along the dune but not the overall dune profile.

To measure the degree of mixing, we use the concept of mixing entropy (see for example Wen et al., 2015 for an application to granular mixing). In a particular region of space, the mixing entropy S for a binary mixture with a x_1 fraction of type 1 particles and a $x_2 = 1 - x_1$ fraction of type 2 particles is defined as

$$S = x_1 \ln x_1 + x_2 \ln x_2. \tag{13}$$

For an empty volume (i.e., $x_1 = x_2 = 0$) or for a volume that contains only one type of particles (e.g., $x_1 = 1$ and $x_2 = 0$) the mixing entropy is equal to zero. For a volume with same number of particles of each type (i.e., $x_1 = x_2 = 0.5$) the entropy is maximum. This measure can be applied to small cells across the domain to create a map showing the degree of mixing in the system. We have divided the slot domain in 120 cells in the vertical direction and 240 cells in the horizontal direction. The mixing entropy S_{ij} was calculated in each cell defined by the indexes i (horizontal) and j (vertical). The results are shown as a color map in Fig. 11, where the entropy values were normalized so that the maximum entropy is 1. These color maps measure quantitatively the results that can be inferred from the simulation snapshots of the different injection protocols (see Fig. 9). In Fig. 11(a) we can see that the simultaneous injection of both proppants leads to high values of mixing entropy across the whole dune. For the ceramic–sand and sand–ceramic injections (see Fig. 11(c) and (e)) the zones with high mixing entropy correspond to the interfaces between layers of different particle types.

To obtain the average mixing entropy along the cell length, the entropy of every column i is obtained adding the entropy of every cell j in that column according to (Wen et al., 2015)

$$S_i = \sum_{j=1}^{N_y} n_{ij} S_{ij}, \tag{14}$$

where n_{ij} is the total number of grains in the ij cell and N_y is the number of cells in the vertical direction. It should be noted that the added mixing entropy of a set of cells is different from the mixing entropy of the same volume considered as a single cell. The mixing entropy is sensitive to the size of the basic cell used.

The entropy profiles shown in Fig. 11(b), (d) and (f) are very much in line with the apparent degree of mixing observed by eye on the simulation snapshots (see Fig. 9) and also in the entropy color maps (see Fig. 11, left column). Along with the entropy profiles we also have plotted the concentration of each proppant type n_i/n_T, being n_i the number of particles of type i and n_T the total number of particles in any given column. It is clear that for the simultaneous injection a high mixing entropy is obtained along the whole cell. We can depict only a decay of mixing entropy at the right end of the cell where most of the material is sand. For the ceramic–sand injection, we see a small region near the cell entrance with a high mixing entropy, then, we see a rather continuous decay along the cell except for a peak at $x/h = 1.25$. We also see that at the right end of the cell there is an increase in the amount of ceramic. This is due to the fact that ceramic proppant was injected first (see middle column of Fig. 9). When sand is injected first, a high value of mixing entropy is observed near the entrance. Then, we see a decay and an increase around $x/h = 1.25$. At the right end of the cell the content of sand reaches the maximum, because sand was injected first (see right column of Fig. 9). For that reason, the mixing entropy drops to zero.
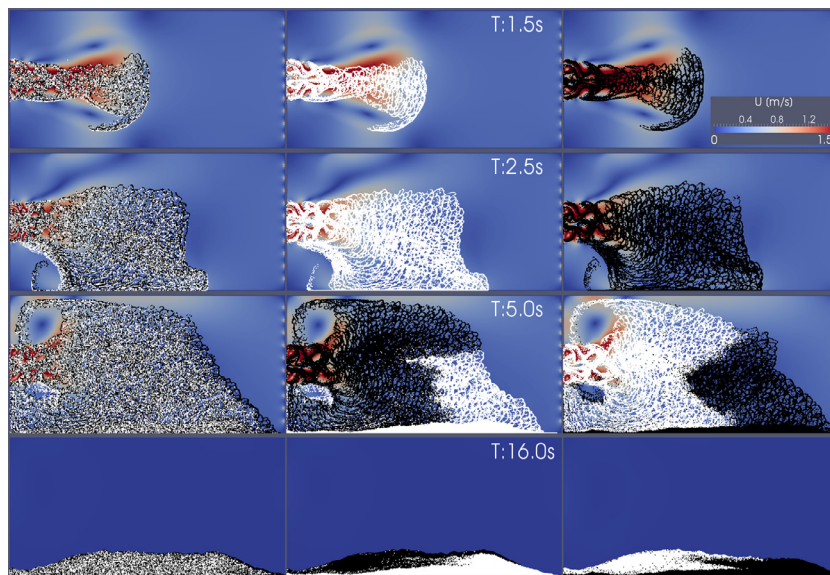
Fig. 9. Snapshots of the simulations for middle injection cluster using three different strategies of mixing 16/30 sand (black dots) and 16/30 ceramic (white dots) proppant particles: simultaneous injection (left column), ceramic before sand (middle column) and sand before ceramic (right column). The color scale corresponds to the magnitude of the fluid velocity in m/s. (For interpretation of the references to color in this figure legend, the reader is referred to the web version of this article.)
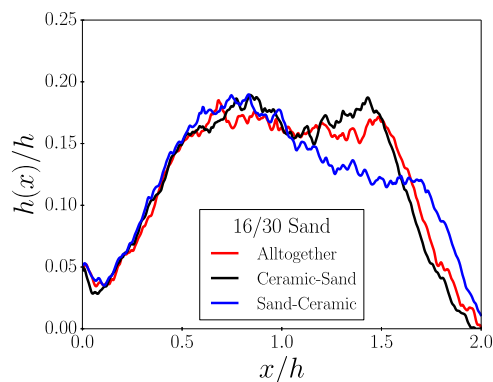

Fig. 10. Dune profiles for middle injection cluster using three different strategies of mixing sand and ceramic of size 16/30. The red curve correspond to the simultaneous injection of both proppant types, black to ceramic–sand and blue to sand–ceramic injection. Lengths are scaled with the height $h = 0.8$ m of the cell. (For interpretation of the references to colour in this figure legend, the reader is referred to the web version of this article.)

6. Discussion

It is important to discuss to what extent the results presented in Section 5 can be extrapolated to field operations. As we explain above, the planar vertical slot considered has been scaled to roughly represent the aspect ratio of a field fracture effectively propped. The inlets and fracture width are similar to the field values. The pumping rate has been selected to yield a mean fluid velocity in the slot of the same order of the one obtained in the field. Since the properties of the fluid phase correspond to water, we expect that the Reynolds number will be similar to slickwater operations.

The proppant particles used in the simulations are somewhat larger than those used in regular field operations. It is a common practice to use sand of mesh 70 and above (i.e., < 0.2 mm in diameter) during the initial phase of the stimulation process. During the last phase, 16/30 ceramic proppant (i.e., 0.4 mm to 1.2 mm) are generally pumped. Instead, we have chosen bigger meshes (16/30

and 20/40) to fill an appreciable portion of the cell using a manageable number of particles, without the need of significant CPU time. These simulations took around 10 days in a workstation using four processors in parallel. Also, we need to mention that in field operations, ceramic proppant would not be injected using slickwater, but a cross-linked gel with strong non-Newtonian behavior.

Although the position of the inlets have an important effect in the proppant placement, one may wonder if some degree of control of the relative position of the fracture and the perforations in the casing is possible. One could control this by placing injection clusters close to geological boundaries (whenever they exist) that have the ability of limiting the growth of the fracture in the vertical direction. This may offer an opportunity for better control of the proppant placement.

Finally, we have to bear in mind that the simulation results discussed correspond to injecting only a portion of what is usually injected in a field operation. Further injection may lead to the reshape of the dune, the formation of a traction carpet and filling of the slot downstream (Kern et al., 1959; Zhang et al., 2017a; Zeng et al., 2016). A study of the complete filling of the slot for different conditions of inlet positions and proppant order would require more CPU demanding simulations. However, these are not out of reach for larger computing resources.

Despite the issues discussed here, the proppant placement we observe is consistent with previous experiments (Sahai et al., 2014; Liu, 2006) and simulations (Zeng et al., 2016; Zhang et al., 2017a; 2017b; 2017c). The CFD–DEM simulations of scaled slots are subjected to the same approximations and scaling done for experimental setups. Hence, most conclusions and extrapolations valid for experimental studies seem to be justified also for the CFD–DEM modeling investigations.

Other authors (Zhang et al., 2017a; Zeng et al., 2016) already proved the advantage of the CFD–DEM method in modeling proppant transport. Our work put emphasis on the importance of the position of the injection clusters and the effect of injecting different proppant types simultaneously and in stages.
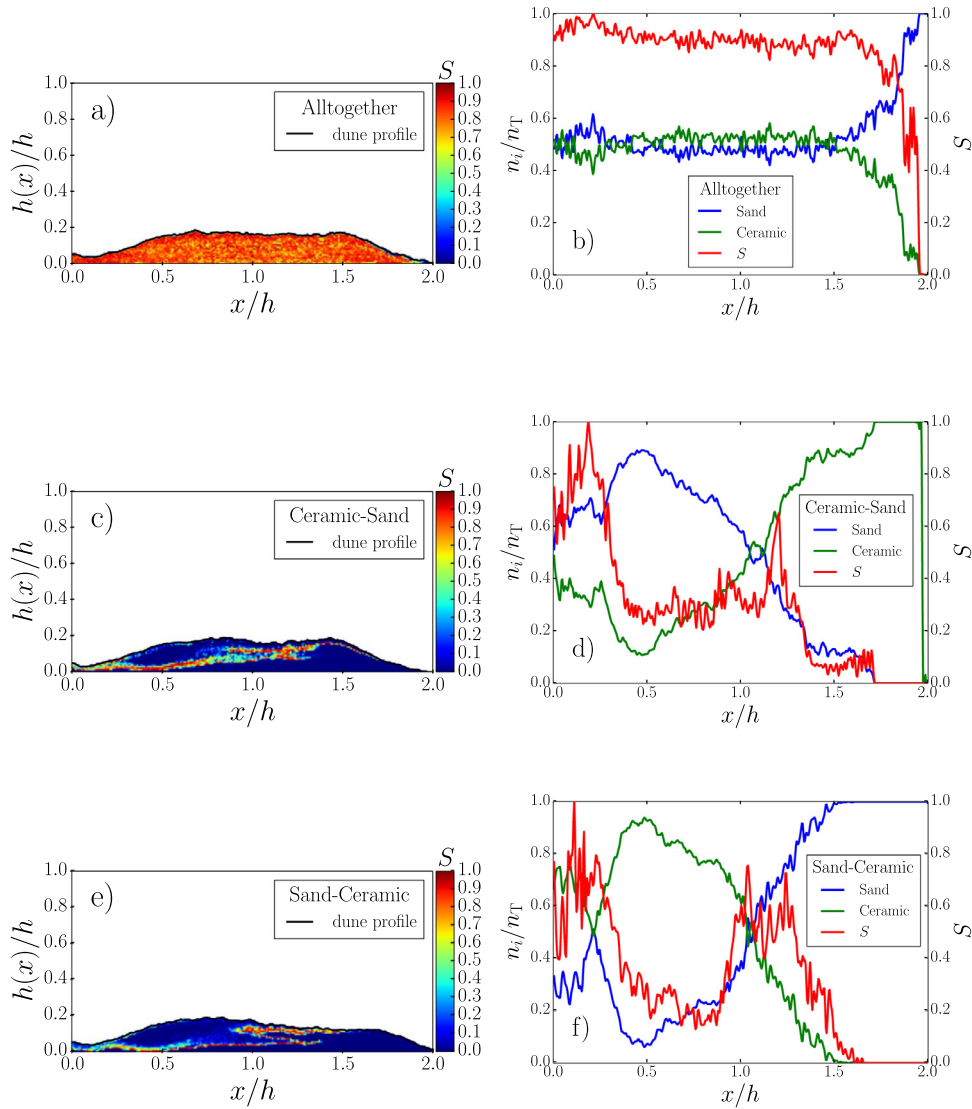
Fig. 11. Entropy of mixing for the deposited dunes in Fig. 9. The color scale corresponds to the normalized mixing entropy. (a) Simultaneous injection of both proppant types. (c)–(e) ceramic before sand and sand before ceramic injection, respectively. On the right column we show the corresponding mixing entropy profiles and concentration of particles n_i/n_T for the deposited dunes. Lengths are scaled with the height $h = 0.8$ m of the cell. (For interpretation of the references to color in this figure legend, the reader is referred to the web version of this article.)

7. Conclusions

We have considered the injection of proppant of different size and density into a vertical cell at different heights using a CFD–DEM modeling approach. The results are consistent with previous experimental and simulation studies at least at a qualitative level.

We have observed that injecting at the top of the cell induces, in general, the most smeared dune in comparison with placing the injection points at the middle or bottom of the slot. Both, bottom and middle injections lead to convection eddies that favor a deposition close to the injection side of the slot.

The usual practice of injecting sand proppant first followed by ceramic has the effect of leaving a widely spread deposition of the light particles in the cell base, on top of which the second layer of particles deposits. This is observed for a cluster injection positioned at mid height in the slot. Injection of both proppant types simultaneously leads to a well mixed dune. Also, for all injection protocols, we can say that approximately the same dune profile is obtained.

We have compared simulations that use different slot lengths. The results of dune profile are remarkably similar. This suggests that experimental devices using not to long slots do not make an important impact on the final distribution of the proppant dunes. Also, we compared simulations using a refined CFD mesh. The results are similar to the ones produced using the coarse CFD mesh, suggesting that the coarse mesh is fine enough to reproduce the system dynamics.

Finally, we have used a measure of the degree of mixing for mixed proppant injections based on the concept of mixing entropy. This parameter seems to be a very simple and suitable way to measure the degree of mixing observed in the dune. This helps to depict to what extent different proppants remain segregated in the slot. Well-mixed dunes have less conductivity when a well is put in production, so well-segregated dunes are desirable.

It is important to bear in mind that the actual field conditions during industrial operations may differ from the ones used in this study, particularly with respect to fracture thickness. However, the use of these types of CFD–DEM simulations will be particularly suitable to study complex configurations that are difficult to setup

in experiments. Examples of these are the study of branched fractures and proppant stability on flowback (Shor et al., 2014).

Acknowledgment

References

Alotaibi, M.A., Miskimins, J.L., et al., 2015. Slickwater proppant transport in complex fractures: new experimental findings & scalable correlation. In: SPE Annual Technical Conference and Exhibition. Society of Petroleum Engineers, p. 174828.

Anderson, T.B., Jackson, R., 1967. Fluid mechanical description of fluidized beds. Equations of motion. Ind. Eng. Chem. Fund. 6 (4), 527–539.

Antypov, D., Elliott, J., 2011. On an analytical solution for the damped hertzian spring. EPL 94 (5), 50004.

Barree, R., Conway, M., et al., 2001. Proppant holdup, bridging, and screenout behavior in naturally fractured reservoirs. In: SPE Production and Operations Symposium, 24–27 March, Oklahoma City, Oklahoma. Society of Petroleum Engineers, p. 67298.

Basu, D., Das, K., Smart, K., Ofoegbu, G., 2015. Comparison of Eulerian–Granular and discrete element models for simulation of proppant flows in fractured reservoirs. ASME 2015 International Mechanical Engineering Congress and Exposition. American Society of Mechanical Engineers. V07BT09A012–V07BT09A012

Blyton, C.A., Gala, D.P., Sharma, M.M., et al., 2015. A comprehensive study of proppant transport in a hydraulic fracture. In: SPE Annual Technical Conference and Exhibition, 28–30 September, Houston, Texas, USA. Society of Petroleum Engineers, p. 174973.

Bokane, A., Jain, S., Deshpande, Y., Crespo, F., et al., 2013. Computational fluid dynamics (CFD) study and investigation of proppant transport and distribution in multistage fractured horizontal wells. In: SPE Reservoir Characterization and Simulation Conference and Exhibition, 16–18 September, Abu Dhabi, UAE. Society of Petroleum Engineers, p. 165952.

Brilliantov, N.V., Spahn, F., Hertzsch, J.-M., Pöschel, T., 1996. Model for collisions in granular gases. Phys. Rev. E 53 (5), 5382.

Cundall, P.A., Strack, O.D., 1979. A discrete numerical model for granular assemblies. Gᴇotechnique 29 (1), 47–65.

Di Felice, R., 1994. The voidage function for fluid-particle interaction systems. Int. J. Multiphase Flow 20 (13), 153–159.

Di Renzo, A., Di Maio, F.P., 2005. An improved integral non-linear model for the contact of particles in distinct element simulations. Chem. Eng. Sci. 60 (5), 1303–1312.

Dontsov, E., Peirce, A., 2014. Slurry flow, gravitational settling and a proppant transport model for hydraulic fractures. J. Fluid Mech. 760, 567–590.

Dontsov, E., Peirce, A., 2015. Proppant transport in hydraulic fracturing: crack tip screen-out in kgd and p3d models. Int. J. Solids Struct. 63, 206–218.

Economides, M.J., Nolte, K.G., et al., 1989. Reservoir Stimulation, vol. 2. Prentice Hall Englewood Cliffs, New Jersey.

Ertaş, D., Grest, G.S., Halsey, T.C., Levine, D., Silbert, L.E., 2001. Gravity-driven dense granular flows. EPL 56 (2), 214.

Goniva, C., Kloss, C., Deen, N.G., Kuipers, J.A.M., Pirker, S., 2012. Influence of rolling friction on single spout fluidized bed simulation. Particuology 10 (5), 582–591.

Hager, A., 2014. CFD–DEM on Multiple Scales. An Extensive Investigation of Particle–Fluid Interactions. Johannes Kepler University Linz, Linz.

Hertz, H., 1882. Über die berührung fester elastischer körper. J. für die reine und Angewandte Math. 92, 156–171.

Hirsch, C., 2007. Numerical Computation of Internal and External Flows: The Fundamentals of Computational Fluid Dynamics. Butterworth-Heinemann.

Hu, G., Hu, Z., Jian, B., Liu, L., Wan, H., 2010. On the determination of the damping coefficient of non-linear spring-dashpot system to model hertz contact for simulation by discrete element method. In: Information Engineering (ICIE), 2010 WASE International Conference on, vol. 3. IEEE, pp. 295–298.

Issa, R.I., 1986. Solution of the implicitly discretised fluid flow equations by operator-splitting. J. Comput. Phys. 62 (1), 40–65.

Jasak, H., 1996. Error Analysis and Estimation for the Finite Volume Method with Applications to Fluid Flows. University of London Imperial College.

Kern, L.R., Perkins, T.K., Wyant, R.E., et al., 1959. The mechanics of sand movement in fracturing. J. Petroleum Technol. 11 (07), 55–57.

Kloss, C., Goniva, C., Hager, A., Amberger, S., Pirker, S., 2012. Models, algorithms and validation for opensource DEM and CFD–DEM. Prog. Comput. Fluid Dyn. Int. J. 12 (2–3), 140–152.

Kruggel-Emden, H., Simsek, E., Rickelt, S., Wirtz, S., Scherer, V., 2007. Review and extension of normal force models for the discrete element method. Powder Technol. 171 (3), 157–173.

Kruggel-Emden, H., Wirtz, S., Scherer, V., 2008. A study on tangential force laws applicable to the discrete element method (DEM) for materials with viscoelastic or plastic behavior. Chem. Eng. Sci. 63 (6), 1523–1541.

Li, Y., Xu, Y., Thornton, C., 2005. A comparison of discrete element simulations and experiments for sandpiles composed of spherical particles. Powder Technol. 160 (3), 219–228.

Liu, Y., 2006. Settling and Hydrodynamic Retardation of Proppants in Hydraulic Fractures. University of Texas.

Mack, M., Sun, J., Khadilkar, C., et al., 2014. Quantifying proppant transport in thin fluids: theory and experiments. In: SPE Hydraulic Fracturing Technology Conference, 4–6 February, The Woodlands, Texas, USA. Society of Petroleum Engineers, p. 168637.

Medlin, W.L., Sexton, J.H., Zumwalt, G.L., 1985. Sand transport experiments in thin fluids. In: Annual Technical Conference and Exhibition 14469-07, pp. 55–57.

Mondal, S., Wu, C.-H., Sharma, M.M., 2016. Coupled CFD–DEM simulation of hydrodynamic bridging at constrictions. Int. J. Multiphase Flow 84, 245–263.

Norouzi, H.R., Zarghami, R., Sotudeh-Gharebagh, R., Mostoufi, N., 2016. Coupled CFD–DEM Modeling: Formulation, Implementation and Application to Multiphase Flows. John Wiley & Sons.

Ortiz, A.C., Hryb, D.E., Martínez, J.R., Varela, R.A., et al., 2016. Hydraulic fracture height estimation in an unconventional vertical well in the vaca muerta formation, neuquen basin, argentina. In: SPE Hydraulic Fracturing Technology Conference, 9–11 February, The Woodlands, Texas, USA. Society of Petroleum Engineers, p. 179145.

Palisch, T.T., Vincent, M., Handren, P.J., et al., 2010. Slickwater fracturing: Food for thought. In: SPE Annual Technical Conference and Exhibition, 28–30 September, Houston, Texas, USA. Society of Petroleum Engineers, p. 115766.

Patankar, N., Joseph, D., 2001. Lagrangian numerical simulation of particulate flows. Int. J. Multiphase Flow 27 (10), 1685–1706.

Patankar, N., Joseph, D., Wang, J., Barree, R., Conway, M., Asadi, M., 2002. Power law correlations for sediment transport in pressure driven channel flows. Int. J. Multiphase Flow 28 (8), 1269–1292.

Pöschel, T., Schwager, T., 2005. Computational Granular Dynamics: Models and Algorithms. Springer Science & Business Media.

Sahai, R., Miskimins, J.L., Olson, K.E., et al., 2014. Laboratory results of proppant transport in complex fracture systems. In: SPE Hydraulic Fracturing Technology Conference, 4–6 February, The Woodlands, Texas, USA. Society of Petroleum Engineers, p. 168579.

Settari, A., Price, H., et al., 1984. Simulation of hydraulic fracturing in low-permeability reservoirs. Soc. Petroleum Eng. J. 24 (02), 141–152.

Shäfer, J., Dippel, S., Wolf, D., 1996. Force schemes in simulations of granular materials. J. Phys. I 6 (1), 5–20.

Shor, R.J., Sharma, M.M., et al., 2014. Reducing proppant flowback from fractures: factors affecting the maximum flowback rate. In: SPE Hydraulic Fracturing Technology Conference, 4–6 February, The Woodlands, Texas, USA. Society of Petroleum Engineers, p. 168649.

Snider, D., 2001. An incompressible three-dimensional multiphase particle-in-cell model for dense particle flows. J. Comput. Phys. 170 (2), 523–549.

Tomac, I., Gutierrez, M., et al., 2013. Numerical study of horizontal proppant flow and transport in a narrow hydraulic fracture. 47th US Rock Mechanics/Geomechanics Symposium. American Rock Mechanics Association.

Tong, S., Mohanty, K.K., 2016. Proppant transport study in fractures with intersections. Fuel 181, 463–477.

Tsai, K., Fonseca, E., Lake, E., Degaleesan, S., et al., 2012. Advanced computational modeling of proppant settling in water fractures for shale gas production. SPE J. 18 (01), 50–56.

Tsuji, Y., Kawaguchi, T., Tanaka, T., 1993. Discrete particle simulation of two-dimensional fluidized bed. Powder Technol. 77 (1), 79–87.

Versteeg, H.K., Malalasekera, W., 2007. An Introduction to Computational Fluid Dynamics: The Finite Volume Method. Pearson Education.

Wang, J., Joseph, D.D., Patankar, N.A., Conway, M., Barree, R.D., 2003. Bi-power law correlations for sediment transport in pressure driven channel flows. Int. J. Multiphase Flow 29 (3), 475–494.

Washino, K., Chan, E.L., Miyazaki, K., Tsuji, T., Tanaka, T., 2016. Time step criteria in DEM simulation of wet particles in viscosity dominant systems. Powder Technol. 302, 100–107.

Wen, Y., Liu, M., Liu, B., Shao, Y., 2015. Comparative study on the characterization method of particle mixing index using DEM method. Procedia Eng. 102, 1630–1642.

Woodworth, T.R., Miskimins, J.L., et al., 2007. Extrapolation of laboratory proppant placement behavior to the field in slickwater fracturing applications. In: SPE Hydraulic Fracturing Technology Conference, 29–31 January, College Station, Texas, U.S.A.. Society of Petroleum Engineers, p. 106089.

Xu, B., Yu, A., 1997. Numerical simulation of the gas-solid flow in a fluidized bed by combining discrete particle method with computational fluid dynamics. Chem. Eng. Sci. 52 (16), 2785–2809.

Zeng, J., Li, H., Zhang, D., 2016. Numerical simulation of proppant transport in hydraulic fracture with the upscaling CFD–DEM method. J. Nat. Gas Sci. Eng. 33, 264–277.

Zhang, G., Gutierrez, M., Li, M., 2017. A coupled CFD–DEM approach to model particle–fluid mixture transport between two parallel plates to improve understanding of proppant micromechanics in hydraulic fractures. Powder Technol. 308, 235–248.

Zhang, G., Gutierrez, M., Li, M., 2017. Numerical simulation of transport and placement of multi-sized proppants in a hydraulic fracture in vertical wells. Granul. Matter 19 (2), 32.

Zhang, G., Li, M., Gutierrez, M., 2017. Numerical simulation of proppant distribution in hydraulic fractures in horizontal wells. J. Nat. Gas Sci. Eng. 48, 157–168.

Zhou, Z.Y., Kuang, S.B., Chu, K.W., Yu, A.B., 2010. Discrete particle simulation of particle–fluid flow: model formulations and their applicability. J. Fluid Mech. 661, 482–510.

Zhu, H.P., Zhou, Z.Y., Yang, R.Y., Yu, A.B., 2007. Discrete particle simulation of particulate systems: theoretical developments. Chem. Eng. Sci. 62 (13), 3378–3396.